Chapter 9
Electrostatic Force Microscopy Characterization of Low Dimensional Systems

Yoichi Miyahara, Lynda Cockins, and Peter Grütter

Abstract The electrostatic potential profile is of great importance in nanoscale electronic devices. The effect of the random potential caused by dopants or other defects becomes an increasingly more important problem as device size continues to shrink and as devices exploiting quantum effects emerge. We review the past studies on the potential profile in semiconductor heterostructures by Kelvin probe force microscopy (KPFM) and electrostatic force microscopy (EFM), focusing on the technical aspects of the experiments. We then describe measurements of the spatial and temporal fluctuations of the electrostatic potential in an InP/InGaAs heterostructure sample by EFM and KPFM using frequency modulation mode atomic force microscopy (AFM). We also describe a new EFM technique capable of detecting charge with single-electron resolution and show that such techniques can be used for quantitative spectroscopic measurements of discrete electronic states such as those in quantum dots. Finally, we compare EFM and KPFM with two non-AFM-based scanning probe techniques with highly sensitive potentiometry and electrometry capability.

9.1 Fluctuations of the Electrostatic Potential in Semiconductor Low-Dimensional Structures

It is of great importance to characterize the electrostatic potential profile in systems containing semiconductor heterostructures as various types of electronic devices, such as field effect transistors and semiconductor lasers, are built on such structures. In particular, further miniaturization of such electronic devices down to a few tens of nanometers makes it possible to develop new kinds of electronic devices exploiting quantum effects such as quantum dots and quantum point contacts.

Y. Miyahara (✉) · L. Cockins · P. Grütter
Department of Physics, McGill University, 3600 rue University, Montreal, H3A 2T8, Canada
e-mail: miyahara@physics.mcgill.ca

S. Sadewasser and T. Glatzel (eds.), *Kelvin Probe Force Microscopy*, Springer Series in Surface Sciences 48, DOI 10.1007/978-3-642-22566-6_9,
© Springer-Verlag Berlin Heidelberg 2012

In these nanometer scale devices, the effects of electrostatic potential fluctuations in both space and time become crucial for proper operation. As the operation of the device relies on precise control of the electrostatic potential, which is usually performed by applying external voltages to the gate electrodes, background electrostatic fluctuations, either spatial or temporal, can cause serious undesirable effects. For example, a device may exhibit unexpected behavior, such as the formation of a triple quantum dot in a double quantum dot device [1], and/or low-frequency switching noise [2], both of which greatly degrade device performance. It has also been discussed recently that temporal charge fluctuations can be an important source of decoherence in charge qubits [3, 4].

In the case of silicon Metal-Oxide-Semiconductor Field Effect Transistor (Si-MOS-FET) devices, the situation is similar. As the size of the Si-MOS-FET is reduced to the lower tens of nanometers scale, the device size becomes comparable to the characteristic length of the potential fluctuations caused by randomly placed dopants or charged defects in the silicon oxide and oxide/Si interface. This leads to undesirable effects such as a large variability of device parameters such as the threshold voltage [5]. Temporal random charge fluctuations are also known to cause $1/f$ noise limiting low frequency noise performance. A similar issue has also been identified on graphene-based transistors where the random potential in a supporting substrate (typically SiO_2/Si) limits their performance due to their high sensitivity to the surrounding environment [6]. The effects of the random potential become crucial in attempts to realize Si-MOS-based quantum dots, which are of interest as potential solid-state implementations of quantum computing, because of a possible long coherence time [7]. The use of a random potential to create quantum dots has also been proposed [8].

Kelvin probe force microscopy (KPFM) and electrostatic force microscopy (EFM) are powerful tools for investigating the local electrostatic potential and have been used for characterizing such technically relevant systems as two-dimensional electron gases (2DEG) [9–11], high-κ dielectric films on silicon [12–14], and graphene [15, 16]. KPFM and EFM have also been applied to cross sections of technically relevant heterostructures such as $p-i-n$ junction and multiple quantum well laser diodes. The details can be found in a recent review [17]. Because of its importance in the development of quantum/nano electronic devices, other scanning probe techniques capable of giving similar information have also been developed and successfully applied to various systems [18, 19].

In the following sections, we first review the past KPFM and EFM studies on low-dimensional systems, mainly a 2DEG formed in semiconductor heterostructures. We then describe the observation of random electrostatic potential fluctuations by both dc electrostatic force microscopy (dc-EFM) and KPFM using frequency modulation mode atomic force microscopy (FM-AFM). We discuss an interesting relationship between dc-EFM and KPFM and the implications for topography imaging by FM-AFM. Finally, we present the measurement of temporal fluctuations by dc-EFM as a new application for nanoelectronic device research.

To conclude this chapter, a summary is presented of single-electron sensitive electrostatic force microscopy (e-EFM) and two other scanning probe techniques,

which are not based on AFM: scanning single electron transistor microscopy and scanning charge accumulation microscopy (SCAM).

9.1.1 Kelvin Probe Force Microscopy on Semiconductor Heterostructures

Spatially random potential fluctuations in semiconductor heterostuctures are an important subject of research in two different contexts: one in the development of electronic device applications, and the other in the more fundamental context of the quantum Hall effect (QHE).

The effect of the random potential caused by randomly positioned dopants on a 2DEG was postulated as a source of localized states, which play an essential role in the QHE [20]. Nixon and Davies [21] calculated this effect on a realistic 2DEG numerically and depicted the resulting localized states along with the random potential profile. A large number of experimental investigations have been reported since then. We will briefly review the experimental researches done by KPFM and EFM.

There is a substantial body of literature on the observation of the local potential profile in a 2DEG using AFM [10, 22–29]. These measurements were made on high quality 2DEGs formed in a GaAs/$Al_xGa_{1-x}As$ heterostructure interface at cryogenic temperature. The 2DEGs are located below the surface, typically at a depth of around 100 nm (500 nm in [29]). The local potential profile was measured by either ac electrostatic force microscopy (ac-EFM) or frequency modulation mode KPFM (FM-KPFM).

In ac-EFM, cantilever oscillations are excited by coupling the sample and the AFM tip via an electrostatic force. This force is controlled by applying a time varying (ac) voltage as well as a dc bias voltage between tip and 2DEG [30]. The ac modulation frequency, equal to/near the cantilever resonance frequency, is used to enhance the force detection sensitivity through the high quality factor of the AFM cantilever. When the dc bias voltage is regulated with a feedback circuit such that the electrostatic force signal is minimized, the resulting minimizing voltage can be interpreted as the contact potential difference between the tip and sample. This mode of operation was first proposed by Nonnenmacher et al. [31] and was later referred to as amplitude modulation mode KPFM (AM-KPFM). In order to keep the detection sensitivity constant, the oscillation of the cantilever can be driven by self-excitation and a positive feedback loop [22–26] or a phase lock loop (PLL excitation) [29] with a constant ac modulation amplitude. The self-excitation mode keeps the oscillation frequency at the cantilever resonance frequency even when the resonance frequency, is affected by the tip–sample interaction.

FM-KPFM has also been used for this type of measurement [24, 27, 28, 32]. The cantilever oscillation is self-excited mechanically with a piezoelectric actuator with a positive feedback loop [33]. In this case, the oscillation frequency tracks the cantilever resonance frequency which is being altered by the tip–sample interaction.

The change in the resonance frequency (resonance frequency shift) is a measure of the tip–sample interaction. In FM-KPFM, an ac modulation voltage with frequency well below the cantilever resonance frequency is applied between the tip and sample and the resulting modulation of the resonance frequency shift is detected by a lock-in amplifier [34]. The detected modulation is used as input to a dc potential feedback loop, which minimizes the electrostatic interaction by canceling the contact potential difference. It has been argued that FM-KPFM has a higher spatial resolution while AM-KPFM requires a much smaller ac modulation amplitude because of the enhancement of the force detection sensitivity by the high cantilever Q factor [35].

All the experiments mentioned above were performed with a constant-height mode scan at a tip–sample distance of a few tens of nanometers to reduce the influence from the topography. Here, the properties of buried structures (a 2DEG in this case) were probed using the variety of tecniques mentioned above. Most of the experiments focused on a local voltage distribution, in particular a local Hall voltage profile near the sample edge, which is important to understand the microscopic mechanism of electrical conduction in a 2DEG in the QHE regime. The measured signal due to the local contact potential is a disturbance for these measurements and therefore had to be compensated for by measuring a reference contact potential profile on a separate scan [24, 25] or both contact potential and Hall voltage profiles simultaneously using two different modulation frequencies [22, 23]. Hedberg et al. have demonstrated that the ac-EFM technique can be used to study the spatial variation in the density of states of a deep 2DEG which is located 500 nm below the surface by showing Shubnikov-de Haas oscillation observed in the force signal [29].

Crook et al. have used the AM-KPFM technique to characterize the charge pattern created on the surface of GaAs/$Al_xGa_{1-x}As$ heterostructure samples by controlled contact electrification with an AFM tip [10]. The charge patterns, which remain stable at low temperature, depleted the underlying 2DEG to define quantum electronic devices such as quantum dots and quantum point contacts. The technique is named Erasable Electrostatic Lithography (EEL) as the fabricated devices can be erased by light illumination [36]. They observed dissipating charge on the GaAs surface under illumination as well as a random potential profile in the background at 150 mK [10].

9.1.2 Large Spatial Fluctuations in Electrostatic Potential on Epitaxially Grown InAs/InGaAs/InP Heterostructures Observed by FM-AFM

9.1.2.1 Experimental Details

We have studied the electrostatic potential fluctuations in InAs quantum dot/InGaAs/InP heterostructures with a low-temperature AFM [37]. The samples are epitaxially grown by chemical beam epitaxy [38] and have an InGaAs quantum well (QW) in

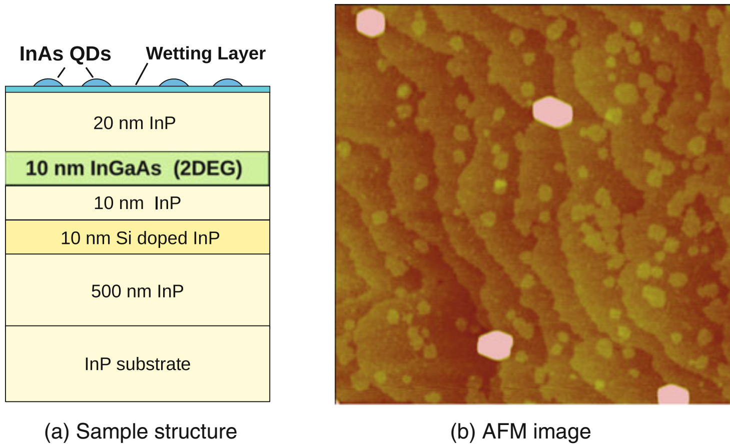

Fig. 9.1 (**a**) Structure of InGaAs/InP heterostructure sample with InAs QDs. (**b**) Topography images of InAs quantum dot sample grown on InP. (1 × 1 μm, height scale 4 nm)

which a two-dimensional electron gas (2DEG) is formed. The $In_{0.47}Ga_{0.53}As$ QW is formed 20 nm below the surface. A 10 nm thick Si-doped InP layer is grown 10 nm below the QW with a 10 nm undoped InP layer in-between. In this system, InAs self-assembled quantum dots (QD) can also be grown on the InP surface due to lattice mismatch. The schematic of the sample structure is shown in Fig. 9.1a.

Figure 9.1b shows a typical surface topography image of the InP/InGaAs/InP heterostructure sample. The image was taken in the amplitude modulation (AM) mode (tapping mode) in air at room temperature by a commercial AFM (Multimode, Veeco). It shows a smooth surface with monoatomic steps and facetted InAs quantum dots.

All the following AFM images were acquired with a home-built low temperature AFM [37] at either 77 or 4.5 K in 3×10^{-3} mbar of He gas atmosphere to better thermalize the sample. We used commercial Si AFM cantilevers (NCLR, Nanosensors). We coated the tip-side of the cantilevers with 20 nm Pt using a 10 nm thick Ti adhesion layer by sputtering to ensure good electrical conductivity at low temperature. The nominal resonance frequency of the coated cantilevers is 160 kHz and the quoted spring constant is $40 \sim 50\,\mathrm{N\,m^{-1}}$. The quality factor, Q, of the cantilevers is typically 8,000 at room temperature, 30,000 at 77 K and 100,000 at 4.5 K. We found that these quality factors were not limited by the dilute He gas atmosphere.

In frequency modulation (FM) imaging mode [33], a commercial oscillator controller and phase-lock loop frequency detector (easyPLLplus, Nanosurf) are used in the self-oscillation mode with a amplitude controller for a constant oscillation amplitude. For AM-mode imaging, the active Q control technique is needed to reduce a high Q factor to an appropriate value (about ∼1,000) [39, 40]. The details of the technique are discussed in the following as this mode of operation (AM-mode

imaging in vacuum) has not been commonly employed. In both operating modes, an oscillation amplitude of 16 $\mathrm{nm_{p-p}}$ was typically used.

9.1.2.2 Active Q-Damped Amplitude Modulation Mode Imaging

In vacuum, the typical Q factor of commonly used AFM cantilevers reaches 10,000 or higher. AM-mode operation is impossible with cantilevers having such a high Q factor because of a long amplitude settling time (e.g., $\tau = Q/\pi f_0 \sim 63\,\mathrm{ms}$ for $Q = 30{,}000$ and $f_0 = 150\,\mathrm{kHz}$) [33]. In order to circumvent this problem, we implemented an active Q control technique [39, 40] to decrease the effective Q factor in order to obtain a fast enough amplitude response for AM-mode operation.

Active Q control has been mostly used to increase the effective Q of cantilevers immersed in liquid environments to achieve higher and more stable imaging [41]. The same technique can also be used to decrease the effective Q by switching the phase shift by 180° in the oscillation control electronics. This active damping technique was applied to increase the imaging speed in AM-mode operation in air where the intrinsic Q of 150 was reduced to 7 [42].

Figure 9.2 shows a schematic diagram of the active Q controlled AM-mode AFM. The added component to the normal AM-mode AFM is the self-excitation loop, which consists of a phase shifter and variable gain amplifier (shown in the box in the figure) to form a feedback loop for the cantilever deflection signal. This feedback loop can be positive or negative depending on the setting of the phase shifter. The positive (negative) feedback leads to an increase (decrease) in effective Q factor.

We use the phase shifter and variable gain amplifier in a commercially available oscillator controller (EasyPLLplus, Nanosurf), which was originally designed to

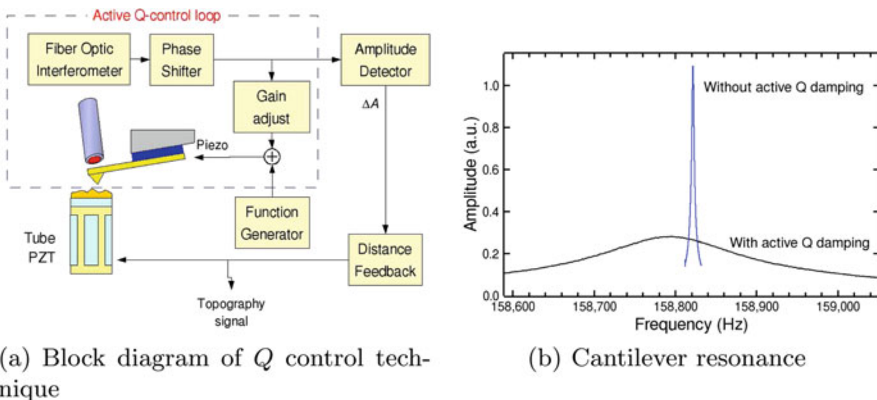

(a) Block diagram of Q control technique

(b) Cantilever resonance

Fig. 9.2 (**a**) Block diagram of active Q-damped amplitude modulation mode AFM. (**b**) Cantilever resonance curves with/without active Q damping. $Q = 59,000$ before and $Q = 960$ after active Q damping

be used for FM-mode operation. An external summing amplifier was used to add the self-excitation signal to an external drive signal from a signal generator. In order to decrease the effective Q, we first adjust the phase so that the cantilever starts self-oscillating at its resonance frequency by minimizing the drive amplitude as is done in the normal FM-mode operation. Then we invert the phase by 180° to switch to active-Q damping mode operation. The self-oscillating loop is now working as a negative feedback as opposed to the previous case, and the higher feedback gain leads to a lower effective Q factor. We reduced an intrinsic Q factor of more than 10,000 to an effective Q factor of less than 1,000 (Fig. 9.2b), which enables a reasonable scanning speed using typical AFM cantilevers with a resonance frequency of a few 100 kHz.

A low-pass filter is often needed to suppress the oscillation from higher oscillation modes (usually from second flexural mode). The highest possible gain (which means the minimum possible Q) is limited by the self-oscillation of other mechanical vibrational modes, most often those of the cantilever itself.

9.1.2.3 Comparison Between Topographic Images Taken in FM-Mode and AM-Mode

Figure 9.3a, b shows the topography of the InAs QD sample in constant-amplitude AM-mode with active Q damping and in constant-frequency shift (Δf) FM-mode in vacuum at 77 K, respectively. The AM-AFM image (Fig. 9.3a) shows clear topographic structure with monoatomic steps and facetted QDs, which is comparable to the one shown in Fig. 9.1b. In FM-mode imaging, however, it was impossible to get images such as shown in Fig. 9.3a since a more negative Δf set-point led to unstable imaging due to the intermittent stops of the cantilever oscillation induced by the sudden topographic change associated with the QDs.

The importance of the electrostatic force in topographic imaging with FM-AFM was recognized as soon as the FM-AFM technique was used for high-resolution topography imaging. A constant dc bias voltage is usually applied between the tip and sample to minimize the electrostatic force while imaging. This minimization technique was often found to be sufficient for high-resolution FM-AFM imaging of homogeneous samples [43].

On the InAs QD/InGaAs/InP heterostructure sample, however, it is not enough to apply a constant dc bias voltage to get real topographic images of good quality with FM-mode. Fig. 9.3b shows a typical topography image of the same sample as shown in Fig. 9.1b taken with FM-mode at a bias voltage of −0.3 V, which minimizes the average electrostatic interaction. The image looks more blurry and the flat terraces in Fig. 9.3 show much more roughness. As we will see later, it turns out that these features originate from spatially inhomogeneous electrostatic interactions, which exhibit a large spatial variation. This is in contrast to imaging in the AM-mode, where the tip and sample were simply electrically connected (i.e., zero bias voltage applied) and thus no particular attempt was made to minimize the electrostatic force. The AM-AFM imaging mode is not as sensitive to the

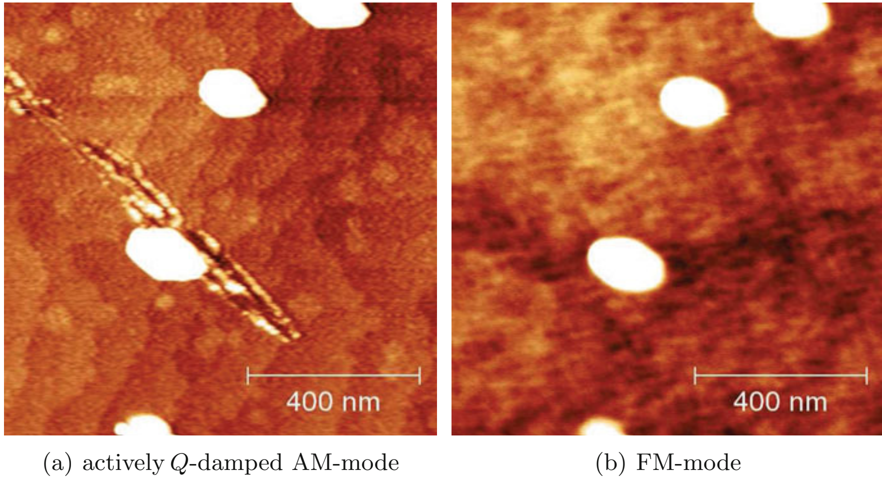

(a) actively Q-damped AM-mode (b) FM-mode

Fig. 9.3 Topography images of an InAs quantum dot sample grown on InP/InGaAs/InP heterostructure substrate taken at 77 K. (**a**) Taken by AM-mode with active Q damping. The effective Q was 960 and the amplitude set-point was 98% of the free oscillation amplitude. The excitation frequency was chosen to be the resonance frequency of the cantilever ($f_0 = 158{,}790$ Hz). The scratch was made by an accidental tip crash. (**b**) FM-mode image taken at 77 K on the same area as (**a**). ($\Delta f = -7.5$ Hz, $V_{\text{bias}} = -0.3$ V, $Q = 56{,}000$). Both images were taken in the same experimental run ((**b**) first and then (**a**)) with the same tip and the same oscillation amplitude of 16 $\text{nm}_{\text{p-p}}$. The height scale is 2 nm for both images

electrostatic force as FM-AFM. This different sensitivity to the electrostatic force can easily be qualitatively understood. In the AM-AFM case, the tip goes into the repulsive interaction regime (intermittent contact) for typical operating conditions (assuming an amplitude set point ∼90% of the free amplitude and a small dc bias voltage) [44]. Under these conditions, the resulting change in oscillation amplitude is largely determined by short-range interaction and thus is less sensitive to the longer-range electrostatic interaction. The FM-AFM, however, is sensitive to long-range electrostatic interactions. If not compensated for, it is often difficult to take images on heterogeneous samples because the cantilever oscillation can become unstable.

We conclude that AM-imaging mode with active Q damping is a useful operating mode in vacuum to obtain the real topography of electrostatically heterogeneous samples with minimal influence of the electrostatic force.

9.1.2.4 Bias Dependence of FM-AFM Image

In order to clarify the origin of the apparent roughness found in the FM-AFM image (Fig. 9.3b), we investigated the topography images as a function of the bias voltage, V_{bias}. Figure 9.4 shows the constant Δf topography images taken at

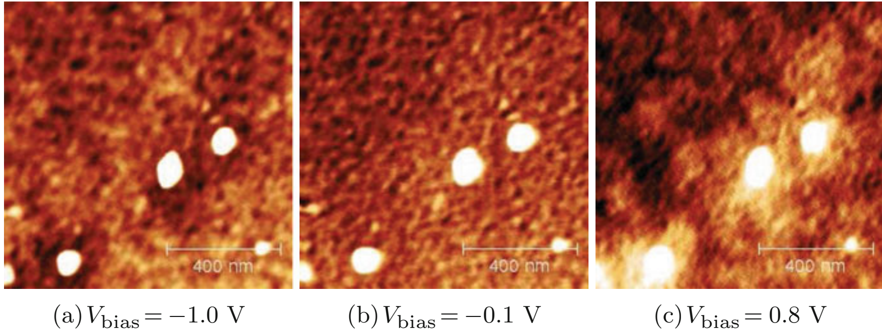

(a) $V_{\text{bias}} = -1.0$ V (b) $V_{\text{bias}} = -0.1$ V (c) $V_{\text{bias}} = 0.8$ V

Fig. 9.4 Constant frequency shift topography images of an InAs quantum dot/InP heterostructure sample taken at different bias voltages, V_{bias} at $T = 4.5$ K. (**a**) $V_{\text{bias}} = -1.0$ V and $\Delta f = -2.43$ Hz, (**b**) $V_{\text{bias}} = -0.1$ V and $\Delta f = -0.69$ Hz, (**c**) $V_{\text{bias}} = 0.8$ V and $\Delta f = -3.01$ Hz, The mean tip-sample distance was set to be the same for all the images. The height scale is 2 nm for all the images

different V_{bias}. The mean tip-sample distance was set to be the same for all the images by choosing the Δf set-point (determined from a reference Δf-V_{bias} curve taken at a position over the sample (the similar curve as shown in Fig. 9.5d). All of the images in Fig. 9.4 show the characteristic apparent roughness well above the instrumental noise floor. We notice many similar features in the background roughness. Furthermore, the contrast of the features is bias voltage dependent. In particular, the background around the QDs increases from Fig. 9.4a–c, indicating the contrast is of electrostatic origin.

The same behavior is observed on the sample without InAs QDs. Figure 9.5 shows the constant Δf topography images taken at $V_{\text{bias}} = 1.0, -0.6$ and -1.0 V. These images could be taken at a more negative Δf set-point (smaller tip-sample distance) than the previous images because there are no QDs on the sample surface. This explains why Fig. 9.5b shows a more clearly resolved surface topography with atomic steps. ($V_{\text{bias}} = -0.6$ V corresponds to the minimizing V_{bias} deduced from a $\Delta f - V_{\text{bias}}$ curve.) On the other hand, Fig. 9.5a shows a random pattern and Fig. 9.5c shows a mixture of the topography in (b) and the random pattern in (a).

With this set of images, we demonstrate that the random background pattern clearly shown in Fig. 9.5a originates from the random spatial fluctuation of the surface potential. In passing we point out that increasing V_{bias} increases the apparent topographic roughness and can eventually mask the underlying topography completely. This can be understood as follows. The force acting on an AFM probe can be expressed as $F_{\text{tot}} = F_{\text{cap}} + F_{\text{res}}$, where the first term is the capacitive force and the second term is the force independent of the applied bias voltage and is due to all other force components. F_{res} is usually dominated by chemical bonding forces and van der Waals forces and is responsible for real topographic information. The capacitive force, F_{cap}, can be derived from the partial derivative of the total electrostatic energy (energy stored in the tip-sample system plus the work done by

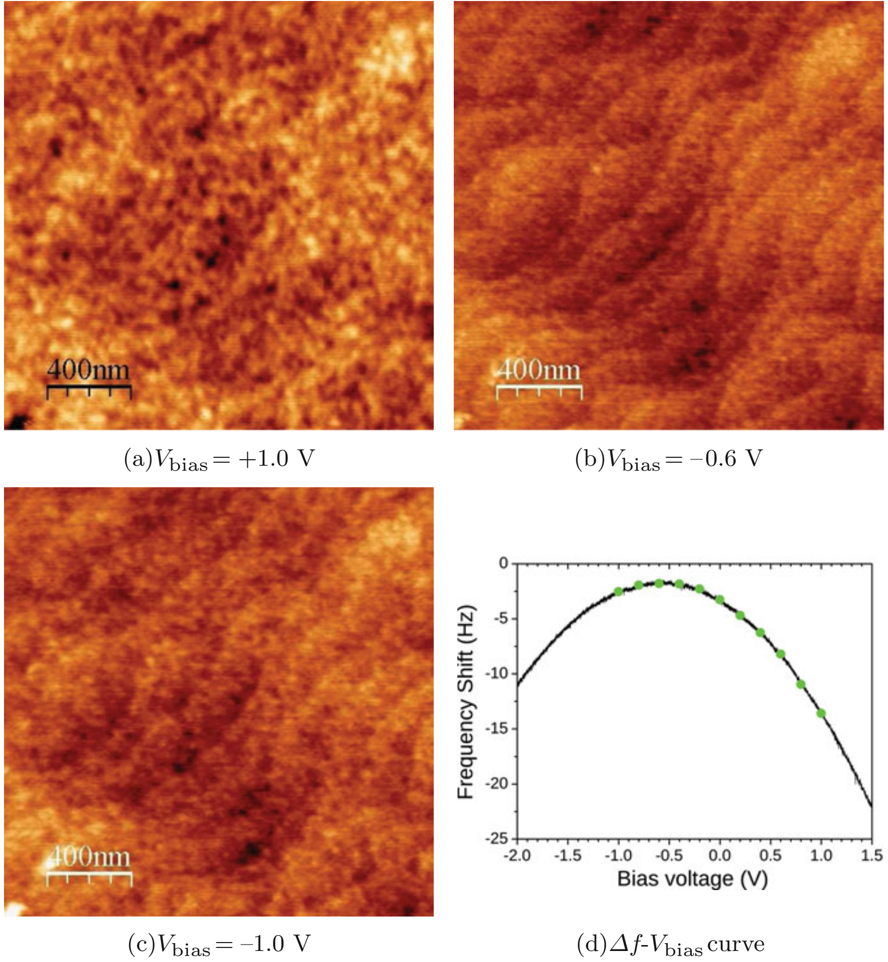

Fig. 9.5 Constant frequency shift topography images of InP heterostructure sample taken at different bias voltages, V_{bias} at $T = 77$ K. (**a**) $V_{\mathrm{bias}} = +1.0$ V and $\Delta f = -13.7$ Hz, (**b**) $V_{\mathrm{bias}} = -0.6$ V and $\Delta f = -1.83$ Hz, (**c**) $V_{\mathrm{bias}} = -1.0$ V and $\Delta f = -2.33$ Hz, The mean tip-sample distance was set to be the same for all the images. (**d**) Δf-V_{bias} curve used for setting the tip-sample distance. The curve is taken at a position on the sample and the Δf set-point is determined the curve to set the same distance at each V_{bias}

the voltage source) [45] and can thus be expressed as:

$$F_{\mathrm{cap}}(z, V_{\mathrm{bias}}) = -\frac{1}{2}\frac{\partial C}{\partial z}(V_{\mathrm{bias}} - V_{\mathrm{CPD}}(x, y))^2 \tag{9.1}$$

for a metallic tip and sample under a constant bias voltage condition, where z is the tip-sample distance and (x,y) is the lateral position of the tip. This expression

is also valid for systems containing dielectric materials between the tip and counter electrode if there are no fixed charges (cf. system with fixed charges can be described by (9.3)). For a small oscillation amplitude, the frequency shift is expressed as $\Delta f = \frac{f_0}{2k}\frac{\partial F}{\partial z}$. The total frequency shift is $\Delta f_{\text{tot}} = \Delta f_{\text{res}} + \Delta f_{\text{cap}}$, where

$$\Delta f_{\text{cap}} = -\frac{f_0}{4k}\frac{\partial^2 C}{\partial z^2}(V_{\text{bias}} - V_{\text{CPD}}(x, y))^2. \tag{9.2}$$

The constant Δf topography images include "electrostatic roughness" caused by the spatially nonuniform local contact potential difference, $V_{\text{CPD}}(x, y)$. The effect of the spatially varying capacitance $\partial^2 C/\partial z^2(x, y)$ is small in a sample with little variation in topography. Therefore, changing V_{bias} changes the contribution of the electrostatic force to the total apparent topography as shown in Fig. 9.5. Although the importance of this effect has already been demonstrated previously on inhomogeneous samples [46, 47] as a contrast inversion in the apparent topography, such an inversion is correlated with the real topographic feature of the samples. In the case of the InP heterostructure sample, however, the electrostatic roughness appears random and uncorrelated with the real surface topography. It is important to realize that the electrostatic roughness can overwhelm the real topography, leading to a complication in interpreting the observed topography taken with FM-mode.

9.1.2.5 Relation Between dc-EFM Contrast and Surface Potential

In order to prove the nature of the electrostatic roughness observed in Fig. 9.5, we performed FM-KPFM imaging on the same surface just after taking the images in Fig. 9.5. We notice a significant resemblance between the V_{CPD} image (Fig. 9.6b) and the topography image taken with $V_{\text{bias}} = +1\,\text{V}$ (Fig. 9.5a). In order to compare the V_{CPD} image with the electrostatic contrast of the topography image (Fig. 9.5a) more clearly, the topography image taken at the minimizing potential ($V_{\text{bias}} = -0.6\,\text{V}$) (Fig. 9.5b) is subtracted to remove the topographic contribution. The resulting difference image (Fig. 9.6d) strikingly resembles the V_{CPD} image obtained by FM-KPFM. This similarity allows us to conclude that the observed electrostatic contrast in the dc-EFM image indeed reflects the spatially varying contact potential difference, $V_{\text{CPD}}(x, y)$. In fact, a constant Δf image taken with a substantial V_{bias} applied can be regarded as a dc electrostatic force microscopy (dc-EFM) image as the total force is dominated by the capacitive force, F_{cap}.

We can use dc-EFM to observe the spatial fluctuations of the surface potential with a higher spatial resolution than FM-KPFM because $F_{\text{cap}}(x, y)$ can be increased by increasing V_{bias}, leading to a higher sensitivity to $V_{\text{CPD}}(x, y)$. KPFM imaging mode, however, is necessary for quantitative measurement of surface potentials. A spatial resolution of $\sim$ 20 nm is achieved in Fig. 9.6d using the subtraction of dc-EFM images acquired at different biases. A higher scanning speed can be achieved in dc-EFM than FM-KPFM because it is not limited by the slow response of the Kelvin feedback loop. Finally, a further potential advantage of dc-EFM over FM-KPFM is that there is no need for ac modulation which induces an additional

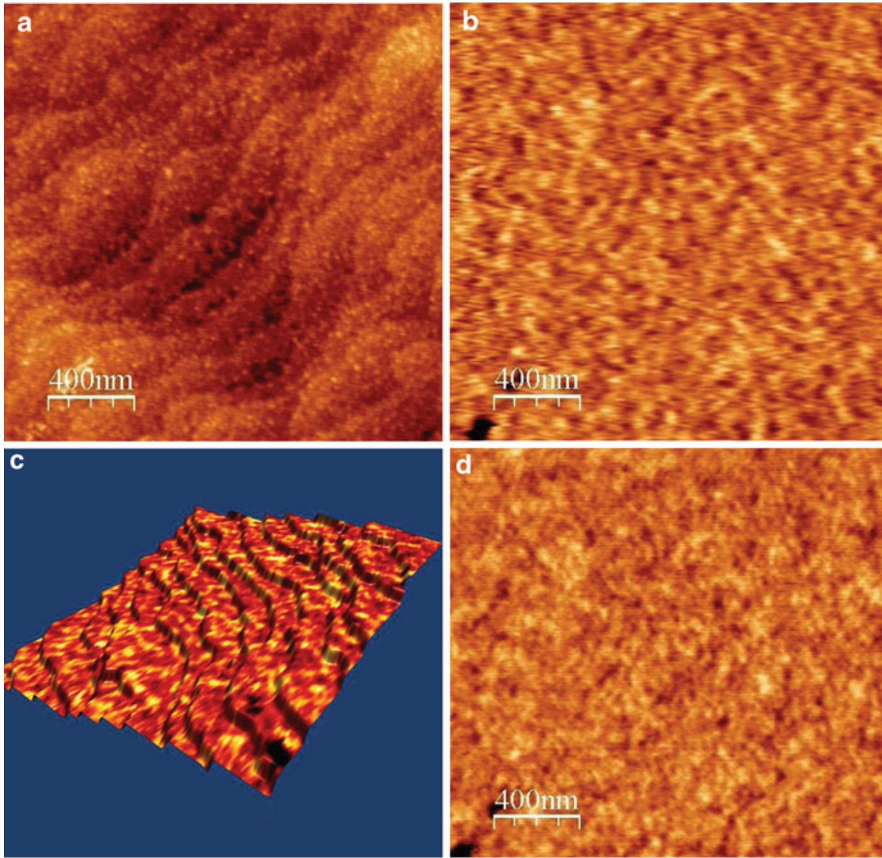

Fig. 9.6 (**a**) Topography and (**b**) surface potential images on an InP 2DEG sample by FM-KPFM. (**a**) and (**b**) were taken simultaneously. Height scale of (**a**) and (**b**) are 2 nm and 1.2 V, respectively. ($\Delta f = -13$ Hz, $V_{ac} = 1\,V_{p-p}$ with the modulation frequency of 1 kHz.) (**c**) Surface potential image (**b**) overlaid as a color code on the smoothed topography image (**a**). (**d**) Difference image of the topography images taken at $V_{bias} = +1.0$ V (Fig. 9.5a) and $V_{bias} = -0.6$ V (Fig. 9.5b)

electrostatic force component ($\frac{1}{2}\frac{\partial C}{\partial z}V_{ac}^2$) [48]. Since this component cannot be canceled by the Kelvin feedback, it can mask the electrostatic force component carrying V_{CPD} information or can introduce an artifact caused by the topography [49].

The potential fluctuations observed in Fig. 9.6b are as high as $\sim 1\,V_{p-p}$. As shown in the V_{CPD} map overlaid on the topography (Fig. 9.6c), there is no clear correlation between the V_{CPD} and the topography, indicating that the origin of the fluctuations is below the surface. By combining this information with the higher spatial resolution of dc-EFM, we can deduce a local electric field on the order of $10^7\,\mathrm{V\,m^{-1}}$. An electric field of this magnitude is large enough to influence the orientation of

molecules on the surface as well as the behavior of charged carriers on/below the surface.

Similar spatial surface potential fluctuations have been observed on high-κ dielectric materials [12–14] and partially oxidized Si(111)7 × 7 surfaces [50]. These kinds of experiments could benefit from the described combination of dc-EFM and FM-KPFM techniques.

9.2 Temporal Fluctuations of the Surface Potential Under Light Illumination

The dc-EFM technique can also be used for measuring the temporal fluctuations of the surface potential [51]. Figure 9.7a, b show dc-EFM topography images taken on InAs QD/InP with 780 nm laser irradiation on (a) and off (b). The image with the

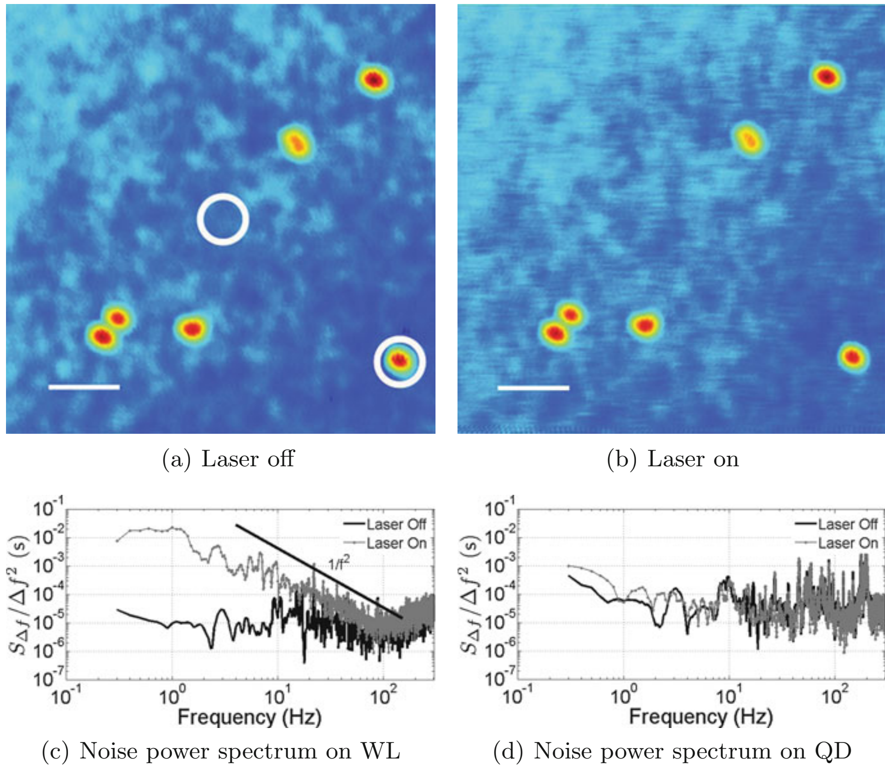

(a) Laser off (b) Laser on

(c) Noise power spectrum on WL (d) Noise power spectrum on QD

Fig. 9.7 Effect of laser irradiation on dc-EFM topography. (**a**) Laser on and (**b**) off. Both images were taken with constant frequency shift ($\Delta f = -31.66$ Hz) with $V_{\text{bias}} = 2$ V at 4.5 K. Scale bars = 200 nm. The EFM image with the laser on (**b**) shows noise (streaks) along the fast scan (horizontal) direction. (**c**) Power spectrum density (PSD) of Δf signal taken over the WL (circled in the center of (**a**)). (d) PSD over the QD (lower circle in (**a**)). From [51]

laser illumination (b) shows many streaks along the fast scan (horizontal) direction. The streaks are found to be caused by fluctuations in the electrostatic force as it mostly disappears in the image taken with $V_{\text{bias}} = V_{\text{CPD}}$ (image not shown).

The noise in the frequency shift, Δf, was characterized by acquiring Δf over the QD and the wetting layer (WL) for 10 s at a constant tip–sample distance of approximately 9 nm. The power spectrum density (PSD) of the Δf noise shows an increase in the low frequency range (<100 Hz) with laser irradiation over the WL but not the QD (Fig. 9.7c, d). The low frequency part of the PSD follows a $1/f^2$ dependence indicating generation-recombination (G-R) noise [52] from photo-excited electron-hole pairs. The spatial separation of electron-hole pairs by the built-in electric field in the space-charge layer leads to the relaxation of the surface band bending, which leads to the fluctuating electrostatic force [53].

Figure 9.8 shows the position dependence of the G-R noise around the QD. It demonstrates that the spatial resolution of the noise measurement by dc-EFM can be as good as 20 nm, which is limited by the tip diameter. The lack of G-R noise over the QDs can be explained by the strong confinement potential of the QD preventing the spatial separation of electron-hole pairs.

In some locations on the WL, random telegraph noise was observed for lower light intensities as shown in Fig. 9.8b. Here, the noise arises from a few fluctuating charges due to trapping and detrapping of localized defect states. The trapping and recombination dynamics of the photo-excited carriers is of great importance in developing photovoltaic devices [54]. The local noise measurement by EFM along with its topography imaging capability can be very useful in the characterization of these devices and their constituent materials.

Low frequency noise measurements with EFM have also been employed to investigate the dynamics of glassy polymers such as the dielectric relaxation and fluctuation [55–59]. In these experiments, the dc-EFM technique was used to measure the Δf noise, which originated from thermal fluctuations of molecular polarization in polymer film samples. A tip–sample distance of typically 20–50 nm

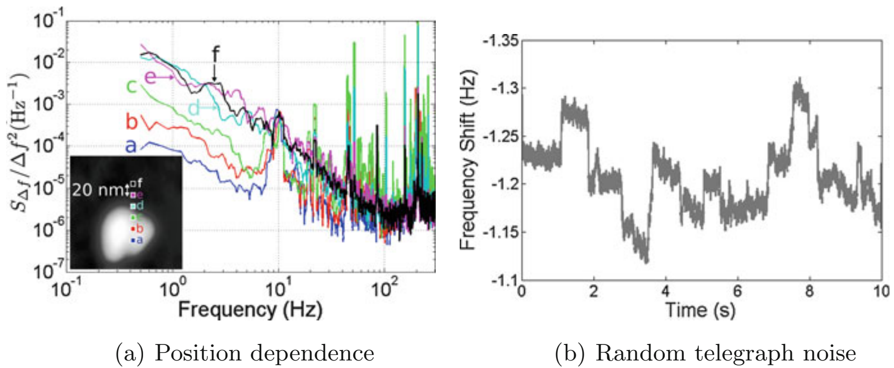

(a) Position dependence

(b) Random telegraph noise

Fig. 9.8 Position dependence of Δf noise. (**a**) PSD of Δf noise taken around the QD. (**b**) Random telegraph noise in Δf observed on WL for low light intensity. From [51]

was used to detect only the long-range electrostatic interaction. Vidal Russell and Israeloff observed the unusual time dependence in the PSD spectra of the Δf as well as occasional occurrences of a random telegraph signal [56]. They ascribe these observations to the switching of configurations in individual molecular clusters. Crider et al. used KPFM to measure local dielectric properties including the dielectric fluctuation. They obtained space-time images of polarization fluctuations on the glassy polymer [57].

Similar noise measurements with a soft cantilever oscillating parallel to the surface have also been reported [58, 59]. Yazdanian et al. measured the Δf noise and the cantilever dissipation caused by electric field fluctuations from the dielectric fluctuations in polymer samples. They observed that the Δf noise is quadratically dependent on the bias voltage and confirmed that their results agree with linear response theory. An interesting connection between the Δf noise and dissipation through fluctuation-dissipation theorem was discussed [59]. As is discussed in [59], Δf noise contains more information on the fluctuating field than the cantilever dissipation as the latter probes only the Fourier component of electric field fluctuation at the cantilever resonance frequency.

9.3 Single-Electron Sensitive Electrostatic Force Microscopy/Spectroscopy

9.3.1 Single-Electron Electrostatic Force Microscopy/Spectroscopy on Quantum Dots

AFM was shown to be capable of detecting electric charge with single-electron charge sensitivity shortly after its invention. Schönenberger and Alvarado demonstrated that AFM can detect the decay of the electric charge deposited in Si_3N_4 film with single-electron resolution by using an ac-EFM technique [60].

More recently, dc-EFM using FM-mode operation has been applied to detect the electric charge stored in QDs with single-electron resolution [61–66]. In these experiments, single-electron tunneling between individual QDs and a back electrode were observed in Δf and the dissipation signal. Imaging as well as spectroscopic measurements of the single-electron charging was demonstrated on various QDs. This technique was demonstrated to be capable of quantitative spectroscopy of electronic energy levels in QDs [66], and possess capabilities such as a sensitivity to degenerate electronic levels (shell structure) and excited-state spectroscopy [67].

Figure 9.9a shows a schematic of the experimental setup used in these experiments. Considering the free energy of the system shown in Fig. 9.9b, the electrostatic force, F_{el}, acting on the AFM tip [64] can be calculated:

$$F_{\mathrm{el}} = \frac{1}{(C_{\mathrm{tip}} + C_{\mathrm{sub}})^2} \frac{\partial C_{\mathrm{tip}}}{\partial z} \left\{ \frac{q^2}{2} - C_{\mathrm{sub}} q V_{\mathrm{B}} + \frac{1}{2} C_{\mathrm{sub}}^2 V_{\mathrm{B}}^2 \right\} \quad (9.3)$$

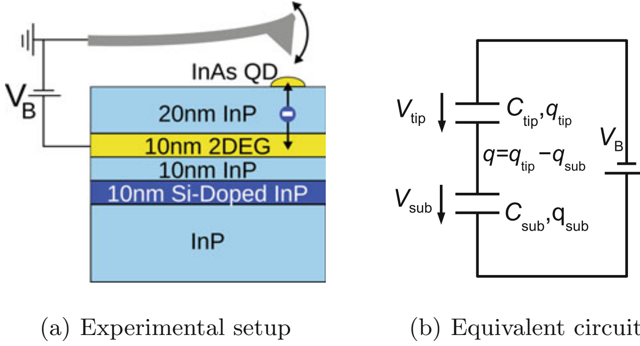

(a) Experimental setup (b) Equivalent circuit

Fig. 9.9 (**a**) Experimental setup for single-electron detection experiment. (**b**) Equivalent circuit of the setup

$$= \frac{1}{2}\frac{\partial C_{\parallel}}{\partial z}\left(\frac{q}{C_{\text{sub}}} - V_{\text{B}}\right)^2, \tag{9.4}$$

where q is the stored charge in the InAs QD and $C_{\parallel} = \frac{C_{\text{tip}}C_{\text{sub}}}{C_{\text{tip}}+C_{\text{sub}}}$. The first term in (9.3) accounts for the interaction between the charge in the QD and its image charge in the tip, but it is negligibly small. The third term accounts for the capacitive force that we have already discussed earlier and shows up as a parabolic background in the Δf-V_{B} curve. The second term is responsible for the detection of the charge in the QD and is referred to as the single-electron force. Although (9.4) resembles the formula for the capacitive force in (9.1), the effect of q on the electrostatic force is qualitatively different as q varies with V_{B} via the electron tunneling through the insulating InP layer. If q is static (i.e., not dependent on V_{bias}), the effect of q can be observed as a shift of the Δf-V_{B} curve. This shift, caused by a single-electron charge, has been observed on single Au atoms on a NaCl/Cu substrate with the dc-EFM technique using a quartz tuning fork AFM where the Au atoms were in two different charge states (neutral Au^0 or Au^-) [68].

At low temperature where the charging energy, $E_{\text{C}} = e^2/2C_{\text{tip}}$ (e: electron charge) is much larger than the thermal energy, $k_{\text{B}}T$, single-electron tunneling occurs at $V_{\text{B}} = \frac{e}{C_{\text{tip}}}(n+1/2)$ (n: integer, number of electrons), leading to a switching of F_{el} such as $F_{\text{el}}(n) \leftrightarrow F_{\text{el}}(n+1)$. This switching of the single-electron force is cycled by the oscillating tip, which effectively modulates the voltage across the InP tunnel barrier. The switching character of F_{el} appear as dips in Δf-V_{B} that are superposed on a parabolic background as shown in Fig. 9.10a. Figure 9.10b shows that the corresponding peaks appear in the dissipation-V_{B} curve as well. The dissipation classically arises from the delayed response of the single-electron force ($\propto q$) due to the finite tunneling rate of the single-electron tunneling process [66, 67]. As is known from the FM-AFM theory [69], Δf and dissipation measure the in-phase and 90° out-of-phase components of $F_{\text{el}}(t)$, respectively. It means that

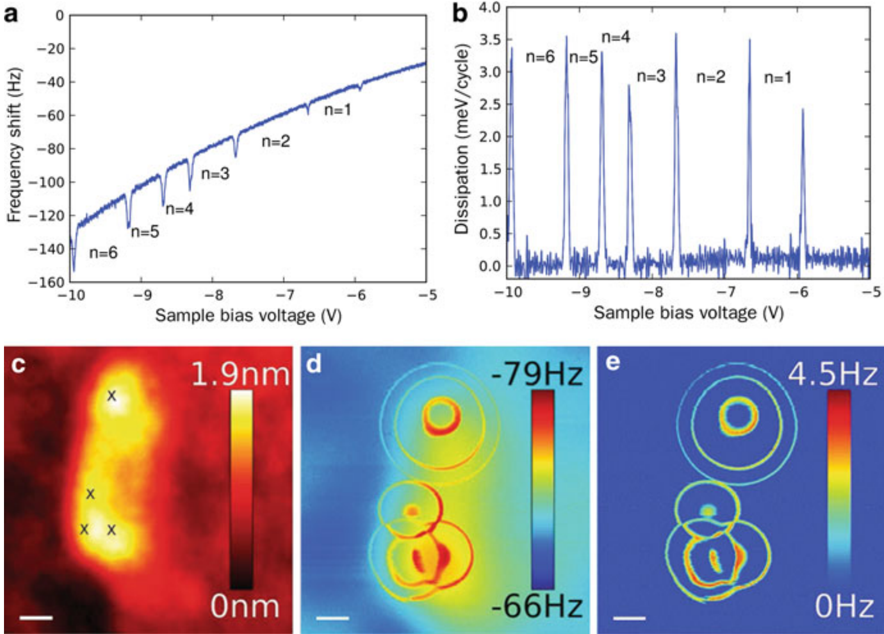

Fig. 9.10 (**a**)Δf-V_B curve and (**b**) Dissipation-V_B curve taken on an InAs QD. n is the number of electrons in the QD. (**c**) Topography of InAs QD. (**d**) Constant-height Δf image of the QD in (**c**). (**e**) Constant-height dissipation image of the QD in (**c**). (**c**) and (**d**) were taken with $V_{bias} = -8$ V at a tip–sample distance of 20 nm. Scale bar in (**c**)–(**e**) is 20 nm

the tunneling rate can be obtained from the relative intensity of the Δf dips and the dissipation peaks.

Figure 9.10d, e show the Δf and dissipation images taken around the QD shown in Fig. 9.10c with a constant V_{bias} of -8 V in constant-height mode scan. Both images show the concentric rings around the QD. These rings correspond to the Δf dips and dissipation peaks in the voltage spectra (Fig. 9.10a, b). The ring furthest from the center corresponds to the first peak ($n = 1$). The rings themselves are contour lines of constant chemical potential in the QD. The better contrast in the dissipation image (e) is due to the fact that the dissipation is not sensitive to the capacitive force (the third term in (9.3)), which gives rise to the background attributed to the topography of the QD observable in Fig. 9.10d.

The imaging capability of this method illustrates the advantage of the technique over conventional transport spectroscopy: It enables one to identify the origin of the peaks when multiple QDs are involved. Without images like Fig. 9.10e, it is cumbersome to identify which peak in the voltage spectra belong to which QD. The images also provide us with a simple way to extract the inter-QD coupling energy, which is of great importance for multiple-QD devices [66]. These images also demonstrate that an individual topographic QD can support multiple confinement potentials.

Similar images of single-electron charging have also been obtained by using scanning gate microscopy (SGM) technique. In SGM, the AFM tip is used only as a mobile local gate and the conductance of the device of interest is measured at each tip position. Similar concentric ring patterns showing single-electron charging in lithographically defined QDs have been reported [61, 70–72]. However, as the SGM technique requires the devices to be wired to external electrodes for conductance measurements, its applicability is rather limited.

9.3.2 Single-Electron Tunneling Force Microscopy/Spectroscopy on Insulator Surfaces

Single-electron tunneling between an AFM tip and individual trap states in insulator surfaces have been observed by Williams's group using the dc-EFM technique [73, 74]. In these experiments, the tip needs to be brought much closer to the sample surface than in the experiments described in the last section. Single-electron tunneling can occur when the tip reaches the closest point to the surface during the oscillation. The single-electron tunneling results in a step-like change in Δf. By applying a dc bias voltage between the tip and backelectrode, a spectroscopic measurement of localized electronic states can be performed. Bussmann and Williams observed localized electronic states in a SiO_2 thin film via identifying sharp steps in the Δf versus bias voltage curves [73, 74] and also observed stochastic single-tunneling events at a fixed bias voltage in the time trace of Δf [74]. Bussmann et al. adopted the FM-KPFM technique for similar measurements and obtained spatial maps of the localized states on SiO_2 [75, 76]. Similar experiment on Au nanoparticles have also been recently reported [77]. This technique is useful for investigating the isolated electronic states that are not tunnel-coupled to nearby electrodes.

9.4 Related Scanning Probe Techniques

For highly sensitive charge or electric potential measurements, there are two other non-AFM based scanning probe techniques: scanning single electron transistor microscopy and scanning charge accumulation microscopy.

9.4.1 Scanning Single Electron Transistor Microscopy

Single-electron transistor microscopy (SSET) was first reported by Yoo et al. [18]. Single electron transistors (SET) are known to be the most sensitive electrometers and have been used for various applications such as single-electron charge detection

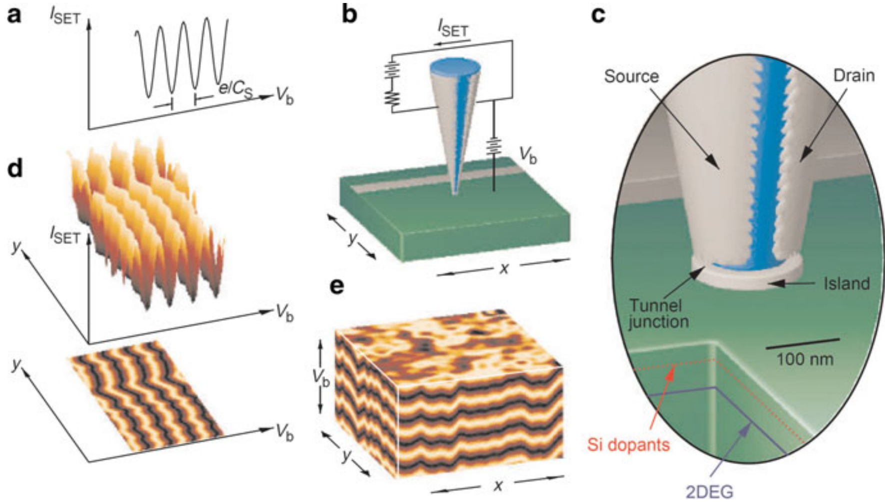

Fig. 9.11 (**a**) Current oscillations of a SET. (**b**) Schematic of SSET technique. (**c**) Magnified view of the SSET tip and the sample structure. (**d**) SET current as a function of the tip position and bias voltage. (**e**) Potential profile of Ga/Al$_x$Ga$_{1-x}$As structure sample at different bias voltages. From [18]. Reprinted with permission from AAAS

in lithographically defined QDs [78] and as a high-sensitivity displacement sensor for a nanoscale mechanical resonator [79]. In the SSET experiment, a SET using an Al/Al oxide tunnel junction is fabricated on a tapered optical fiber tip (Fig. 9.11c). The fiber tip is scanned over the sample surface with a typical tip–sample distance of $\sim$100 nm. A change in electrostatic potential under the probe modulates the current flowing in the SET (Fig. 9.11a). This signal can be interpreted as a surface potential qualitatively or can be used to control the sample bias voltage with a feedback circuit for nullifying the SET current as in KPFM (Fig. 9.11b). Yoo et al. reported a surface potential resolution better than 1 mV and a spatial resolution of $\sim$100 nm, which is limited by the tip size. They observed spatial fluctuations of the surface potential due to the randomly located dopant atoms in a GaAs/Al$_x$Ga$_{1-x}$As heterostructure sample. They also demonstrated that the technique can resolve individual charges created via weak light illumination [18].

The SSET technique has been successfully applied to the microscopic investigation of the QHE, such as the observation of the edge state [80] and localized states [81, 82] predicted theoretically. It has been more recently used to investigate the electron-hole puddles created by the random potential and localization on graphene [83].

In spite of these successes, the technique has not been widely adopted. Some of the drawbacks are that it requires a temperature less than a few Kelvin which limits its application, and that it cannot take good topography images because of the large tip diameter ($\sim$100 nm shown in Fig. 9.11c) . These drawbacks along with a difficult fabrication process keeps this technique from being widely adopted. An attempt has

recently been made to integrate a SET with a quartz tuning fork [84] to overcome these drawbacks but its application has not been reported yet.

9.4.2 Scanning Charge Accumulation Microscopy

Another scanning probe technique with a highly sensitive electrometry capability is known as SCAM [19]. Technically, it is nothing more than an ac current probe with a sharp metallic tip, but a custom-built highly sensitive current amplifier with a cryogenic high electron mobility transistor (HEMT), makes the technique very unique [85]. An ac voltage with a frequency of $\sim$100 kHz and an amplitude 4–6 mV_{rms} is applied between the tip and sample and the resulting ac current is measured by a lock-in amplifier. The output of the lock-in amplifier gives the impedance of the tip–sample system. A charge sensitivity of 0.02 $e/\sqrt{Hz}$ was achieved. As the impedance of the system is influenced mainly by the charge motion in the sample, the technique is sensitive to the electronic properties of buried structures in the sample such as a 2DEG.

SCAM has been applied to interesting phenomena in the QHE regime such as electron puddles [19, 86], the observation of random potentials [19, 87], and the charging of tip-induced single-electron bubbles [88]. The spectroscopy of small numbers of Si dopants in a $GaAs/Al_{0.4}Ga_{0.7}As$ heterostructure have been performed recently and the peculiar electronic levels of Si dopant molecules have been identified [89].

It is worth noting that SCAM can be used for the original Kelvin probe measurement by measuring the ac current induced when the tip is oscillated mechanically (vibrating capacitor method). The technique is based on a simple electrical measurement and thus has the important advantage of being able to sweep the frequency of the ac modulation. It enables the investigation of the frequency response of samples (i.e., impedance measurement), which still remains very difficult with AFM-based techniques which rely on the mechanical resonances of the AFM cantilevers.

As is the case in SSET, the integration of this technique with an AFM would open up interesting applications particularly in the characterization of nanoscale electronic devices.

9.5 Conclusion

We have given an overview of the applications of the EFM and KPFM techniques to semiconductor low-dimensional structures. There has been a substantial body of experimental studies on the potential profile in 2DEGs with both EFM and KPFM. The interest comes mainly from the view point of mesoscopic physics. In particular, a substantial effort has been made to better understand the microscopic mechanism of the QHE. Various experimental techniques have been developed for this end,

most of them for buried structures such as a 2DEG formed in semiconductor heterointerfaces.

We have described the effect of a spatially nonuniform electric potential on FM-mode imaging. We have shown that constant Δf topography images are sensitive to the electrostatic force and that therefore such images taken under a high bias voltage can be interpreted as a surface potential profile by comparing it with the potential profile taken with FM-KPFM. This imaging mode (dc-EFM) can thus be used to measure the surface potential profile with a higher spatial resolution and signal-to-noise ratio than KPFM imaging. KPFM, however, is necessary for quantitative measurement of the V_{CPD}. We have also demonstrated that the active-Q damped AM-AFM mode can be a useful tool for obtaining good topography resolution of samples with tall topographic features such as QDs.

Charge noise measurements by dc-EFM have been discussed. This technique allows to investigate the dynamics of fluctuating charges and thus can be instrumental in characterizing electronic and photovoltaic devices where the dynamics of charge carriers is essential. The effect of fluctuating charges on the decoherence of charge-based qubits can also potentially be addressed by this technique.

Finally, we described single-electron sensitive charge sensing measurements. The single-electron charging spectroscopy described in Sect. 9.3 allows the quantitative determination of energy levels in a quantum system such as a QD and provides the tunneling rate to a nearby electrode. The imaging capability of this technique is helpful to understand the complex charging spectra from multiple QDs and can be used to determine the coupling between QDs. The underlying physics in the technique is of fundamental interest in the emerging field of nanoelectromechanical systems [90] as the interaction between the oscillating AFM tip and tunneling electrons can be described as the back action of a quantum system on the AFM cantilever. This technique can be a versatile tool to study the back action of a quantum system such as quantum dots and individual molecules on a macroscopic system (the AFM cantilever), thus allowing interesting experimental insights into the field of quantum cavities and quantum limited measurements [91].

These EFM-based techniques have two major advantages over other more conventional characterization techniques such as electrical transport measurements. One is that it is a noncontact technique and the other is that it does not require patterned electrodes. These features make it attractive and suitable for investigating nanoscale entities such as quantum dots, defects and individual molecules, which might eventually constitute new types of electronic devices.

References

1. L. Gaudreau, S. Studenikin, A. Sachrajda, P. Zawadzki, A. Kam, J. Lapointe, M. Korkusinski, P. Hawrylak, Phys. Rev. Lett. **97**(3), 36807 (2006). doi:10.1103/PhysRevLett.97.036807. URL http://link.aps.org/doi/10.1103/PhysRevLett.97.036807

2. M. Pioro-Ladrière, J. Davies, A. Long, A. Sachrajda, L. Gaudreau, P. Zawadzki, J. Lapointe, J. Gupta, Z. Wasilewski, S. Studenikin, Phys. Rev. B **72**(11), 1 (2005). doi:10.1103/PhysRevB.72.115331. URL http://link.aps.org/doi/10.1103/PhysRevB.72.115331
3. T. Itakura, Y. Tokura, Phys. Rev. B **67**(19), 195320 (2003). doi:10.1103/PhysRevB.67.195320. URL http://link.aps.org/doi/10.1103/PhysRevB.67.195320
4. J. Bergli, Y.M. Galperin, B.L. Altshuler, New J. Phys. **11**(2), 025002 (2009). doi:10.1088/1367-2630/11/2/025002. URL http://stacks.iop.org/1367-2630/11/i=2/a=025002?key=crossref.937cc0b57df62f086c4461484728f29d
5. A. Asenov, A. Brown, J. Davies, S. Kaya, G. Slavcheva, IEEE Trans. Electron. Dev. **50**(9), 1837 (2003). URL http://ieeexplore.ieee.org/lpdocs/epic03/wrapper.htm?arnumber=1224485
6. J.H. Chen, C. Jang, S. Adam, M.S. Fuhrer, E.D. Williams, M. Ishigami, Nat. Phys. **4**(5), 377 (2008). doi:10.1038/nphys935. URL http://www.nature.com/doifinder/10.1038/nphys935
7. E.P. Nordberg, G.A. Ten Eyck, H.L. Stalford, R.P. Muller, R.W. Young, K. Eng, L.A. Tracy, K.D. Childs, J.R. Wendt, R.K. Grubbs, J. Stevens, M.P. Lilly, M.A. Eriksson, M.S. Carroll, Phys. Rev. B **80**(11), 115331 (2009). URL http://link.aps.org/abstract/PRB/v80/e115331
8. O. Makarovsky, A.G. Balanov, L. Eaves, A. Patanè, R.P. Campion, C.T. Foxon, R.J. Airey, Phys. Rev. B **81**(3), 035323 (2010). doi:10.1103/PhysRevB.81.035323. URL http://prb.aps.org/abstract/PRB/v81/i3/e035323
9. T. Vančura, S. Kičin, T. Ihn, K. Ensslin, M. Bichler, W. Wegscheider, Appl. Phys. Lett. **83**(13), 2602 (2003). URL http://link.aip.org/link/?APL/83/2602/1
10. R. Crook, C. Smith, S. Chorley, I. Farrer, H. Beere, D. Ritchie, Physica E **34**(1–2), 686 (2006). URL http://linkinghub.elsevier.com/retrieve/pii/S1386947706002013
11. G. Valdrè, D. Moro, D. Lee, C.G. Smith, I. Farrer, D.A. Ritchie, R.T. Green, Nanotechnology **19**(4), 45304 (2008). URL http://stacks.iop.org/0957-4484/19/045304
12. R. Ludeke, E. Gusev, J. Appl. Phys. **96**(4), 2365 (2004). URL http://link.aip.org/link/JAPIAU/v96/i4/p2365/s1&Agg=doi
13. J.M. Sturm, A.I. Zinine, H. Wormeester, B. Poelsema, R.G. Bankras, J. Holleman, J. Schmitz, J. Appl. Phys. **97**(6), 63709 (2005). doi:10.1063/1.1870113. URL http://link.aip.org/link/JAPIAU/v97/i6/p063709/s1&Agg=doi
14. J. Sturm, A. Zinine, H. Wormeester, R. Bankras, J. Holleman, J. Schmitz, B. Poelsema, Microelectron. Eng. **80**, 78 (2005). URL http://linkinghub.elsevier.com/retrieve/pii/S016793170500153X
15. S.S. Datta, D.R. Strachan, E.J. Mele, A.T.C. Johnson, Nano Lett. **9**(1), 7 (2009). doi:10.1021/nl8009044. URL http://www.ncbi.nlm.nih.gov/pubmed/18613730
16. Y.J. Yu, Y. Zhao, S. Ryu, L.E. Brus, K.S. Kim, P. Kim, Nano Lett. **9**(10), 3430 (2009). doi:10.1021/nl901572a. URL http://www.ncbi.nlm.nih.gov/pubmed/19719145
17. W. Melitz, J. Shen, A.C. Kummel, S. Lee, Surf. Sci. Rep. **66**(1), 1 (2011). doi:10.1016/j.surfrep.2010.10.001. URL http://dx.doi.org/10.1016/j.surfrep.2010.10.001
18. M.J. Yoo, T.A. Fulton, H.F. Hess, R.L. Willett, L.N. Dunkleberger, R.J. Chichester, L.N. Pfeiffer, K.W. West, Science **276**(5312), 579 (1997). doi:10.1126/science.276.5312.579. URL http://www.sciencemag.org/cgi/doi/10.1126/science.276.5312.579
19. S.H. Tessmer, P.I. Glicofridis, R.C. Ashoori, L.S. Levitov, M.R. Melloch, Nature **392**(6671), 51 (1998). doi:10.1038/32112. URL http://dx.doi.org/10.1038/32112
20. B.I. Halperin, Phys. Rev. B **25**(4), 2185 (1982). doi:10.1103/PhysRevB.25.2185. URL http://link.aps.org/doi/10.1103/PhysRevB.25.2185
21. J. Nixon, J. Davies, Phys. Rev. B **41**(11), 7929 (1990). doi:10.1103/PhysRevB.41.7929. URL http://link.aps.org/doi/10.1103/PhysRevB.41.7929
22. K.L. McCormick, M. T. Woodside, M. Huang, P.L. McEuen, C. Duruoz, J. Harris Jr, Physica B **249–251**, 79 (1998). doi:10.1016/S0921-4526(98)00071-4. URL http://linkinghub.elsevier.com/retrieve/pii/S0921452698000714
23. K. McCormick, M. Woodside, M. Huang, M. Wu, P. McEuen, C. Duruoz, J. Harris, Phys. Rev. B **59**(7), 4654 (1999). doi:10.1103/PhysRevB.59.4654. URL http://link.aps.org/doi/10.1103/PhysRevB.59.4654

24. P. Weitz, E. Ahlswede, J. Weis, K.V. Klitzing, K. Eberl, Appl. Surf. Sci. **157**(4), 349 (2000). URL http://www.sciencedirect.com/science/article/B6THY-403790W-Y/2/45f769f959db7436330cd7e502094690
25. P. Weitz, E. Ahlswede, J. Weis, K.V. Klitzing, K. Eberl, Physica E **6**(1–4), 247 (2000). URL http://www.sciencedirect.com/science/article/B6VMT-3YSY07V-23/2/190637d1d8c82dc273e9b72a66060d52
26. M. Woodside, C. Vale, K. McCormick, PL, Physica E **6**(1–4), 238 (2000). doi:10.1016/S1386-9477(99)00115-0. URL http://linkinghub.elsevier.com/retrieve/pii/S1386947799001150
27. E. Ahlswede, P. Weitz, J. Weis, K.V. Klitzing, K. Eberl, Physica B **298**(1–4), 562 (2001). URL http://www.sciencedirect.com/science/article/B6TVH-4344GH6-41/2/10e88fb8768479257fb665cc0e9d981c
28. F. Dahlem, E. Ahlswede, J. Weis, K. v. Klitzing, Phys. Rev. B **82**(12), 121305(R) (2010). doi:10.1103/PhysRevB.82.121305. URL http://prb.aps.org/abstract/PRB/v82/i12/e121305
29. J.A. Hedberg, A. Lal, Y. Miyahara, P. Grutter, G. Gervais, M. Hilke, L. Pfeiffer, K.W. West, Appl. Phys. Lett. **97**(14), 143107 (2010). doi:10.1063/1.3499293. URL http://link.aip.org/link/APPLAB/v97/i14/p143107/s1&Agg=doi
30. B.D. Terris, J.E. Stern, D. Rugar, H.J. Mamin, Phys. Rev. Lett. **63**(24), 2669 (1989). doi:10.1103/PhysRevLett.63.2669. URL http://link.aps.org/doi/10.1103/PhysRevLett.63.2669
31. M. Nonnenmacher, M.P. O'Boyle, H.K. Wickramasinghe, Appl. Phys. Lett. **58**(25), 2921 (1991). doi:10.1063/1.105227. URL http://link.aip.org/link/APPLAB/v58/i25/p2921/s1&Agg=doi
32. E. Ahlswede, J. Weis, K.V. Klitzing, K. Eberl, Physica E **12**(1–4), 165 (2002). doi:10.1016/S1386-9477(01)00267-3. URL http://linkinghub.elsevier.com/retrieve/pii/S138694770100267373
33. T.R. Albrecht, P. Grutter, D. Horne, D. Rugar, J. Appl. Phys. **69**(2), 668 (1991). doi:10.1063/1.347347. URL http://link.aip.org/link/JAPIAU/v69/i2/p668/s1&Agg=doi
34. S. Kitamura, M. Iwatsuki, Appl. Phys. Lett. **72**(24), 3154 (1998). doi:10.1063/1.121577. URL http://link.aip.org/link/APPLAB/v72/i24/p3154/s1&Agg=doi
35. U. Zerweck, C. Loppacher, T. Otto, S. Grafstrom, L.M. Eng, Phys. Rev. B **71**(12), 125424 (2005). URL http://link.aps.org/abstract/PRB/v71/e125424
36. R. Crook, A.C. Graham, C.G. Smith, I. Farrer, H.E. Beere, D.A. Ritchie, Nature **424**(6950), 751 (2003). doi:10.1038/nature01841. URL http://www.ncbi.nlm.nih.gov/pubmed/12917677
37. M. Roseman, P. Grutter, Rev. Sci. Instrum. **71**(10), 3782 (2000). doi:10.1063/1.1290039. URL http://link.aip.org/link/RSINAK/v71/i10/p3782/s1&Agg=doi
38. P. Poole, J. McCaffrey, R. Williams, J. Lefebvre, D. Chithrani, J. Vac. Sci. Technol. B **19**, 1467 (2001). URL http://link.aip.org/link/?JVTBD9/19/1467/1
39. J. Mertz, O. Marti, J. Mlynek, Appl. Phys. Lett. **62**(19), 2344 (1993). doi:10.1063/1.109413. URL http://link.aip.org/link/APPLAB/v62/i19/p2344/s1&Agg=doi
40. B. Anczykowski, J. Cleveland, D. Krüger, V. Elings, H. Fuchs, Appl. Phys. A **66**(7), S885 (1998). doi:10.1007/s003390051261. URL http://www.springerlink.com/openurl.asp?genre=article&id=doi:10.1007/s003390051261
41. H. Hölscher, D. Ebeling, U.D. Schwarz, in *Q-controlled Dynamic Force Microscopy in Air and Liquids*. NanoScience and Technology (Springer, Berlin, 2007), pp. 75–97. doi:10.1007/978-3-540-37316-2. URL http://www.springerlink.com/content/u201221p217t262k/
42. T. Sulchek, R. Hsieh, J.D. Adams, G.G. Yaralioglu, S.C. Minne, C.F. Quate, J.P. Cleveland, A. Atalar, D.M. Adderton, Appl. Phys. Lett. **76**(11), 1473 (2000). doi:10.1063/1.126071. URL http://link.aip.org/link/APPLAB/v76/i11/p1473/s1&Agg=doi
43. S. Morita, R. Wiesendanger, E. Meyer (eds.), *Noncontact Atomic Force Microscopy* (Springer, Berlin, 2002)
44. R. García, A. San Paulo, Phys. Rev. B **60**(7), 4961 (1999). URL http://link.aps.org/doi/10.1103/PhysRevB.60.4961
45. L N Kantorovich et al., J. Phys.: Condens. Matter **12**(6), 795 (2000). doi:10.1088/0953-8984/12/6/304. URL http://stacks.iop.org/0953-8984/12/i=6/a=304

46. S. Sadewasser, M. Lux-Steiner, Phys. Rev. Lett. **91**(26), 1 (2003). doi:10.1103/PhysRevLett.91.266101. URL http://link.aps.org/doi/10.1103/PhysRevLett.91.266101
47. S.A. Burke, J.M. LeDue, Y. Miyahara, J.M. Topple, S. Fostner, P. Grutter, Nanotechnology **20**(26), 264012 (2009). URL http://stacks.iop.org/0957-4484/20/264012
48. K. Okamoto, Y. Sugawara, S. Morita, Appl. Surf. Sci. **188**(3–4), 381 (2002). URL http://linkinghub.elsevier.com/retrieve/pii/S0169433201009539
49. M. Lee, W. Lee, F.B. Prinz, Nanotechnology **17**(15), 3728 (2006). doi:10.1088/0957-4484/17/15/019. URL http://stacks.iop.org/0957-4484/17/i=15/a=019?key=crossref.495ccf607fae35e6d68dc8dd61337e4a
50. J. Sturm, H. Wormeester, B. Poelsema, Surf. Sci. **601**(19), 4598 (2007). doi:10.1016/j.susc.2007.07.016. URL http://linkinghub.elsevier.com/retrieve/pii/S0039602807007911
51. L. Cockins, Y. Miyahara, P. Grutter, Phys. Rev. B **79**(12), 121309 (2009). URL http://link.aps.org/abstract/PRB/v79/e121309
52. M.J. Deen, F. Pascal, J. Mater. Sci. Mater. Electron. **17**(8), 549 (2006). URL http://www.springerlink.com/index/10.1007/s10854-006-0001-8
53. G. Dumitras, H. Riechert, H. Porteanu, F. Koch, Phys. Rev. B **66**(20), 1 (2002). URL http://link.aps.org/doi/10.1103/PhysRevB.66.205324
54. D.C. Coffey, D.S. Ginger, Nat. Mater. **5**, 735 (2006)
55. L.E. Walther, E.V. Russell, N.E. Israeloff, H.A. Gomariz, Appl. Phys. Lett. **72**(24), 3223 (1998). URL http://link.aip.org/link/?APL/72/3223/1
56. E.V. Russell, N.E. Israeloff, Nature **408**(6813), 695 (2000). URL http://www.ncbi.nlm.nih.gov/pubmed/11130066
57. P.S. Crider, N.E. Israeloff, Nano Lett. **6**(5), 887 (2006). URL http://pubs.acs.org/doi/abs/10.1021/nl060558q
58. S.M. Yazdanian, J.A. Marohn, R.F. Loring, J. Chem. Phys. **128**(22), 224706 (2008)
59. S.M. Yazdanian, N. Hoepker, S. Kuehn, R.F. Loring, J.A. Marohn, Nano Lett. **9**(6), 2273 (2009). doi:10.1021/nl9004332. URL http://dx.doi.org/10.1021/nl9004332
60. C. Schönenberger, S.F. Alvarado, Phys. Rev. Lett. **65**(25), 3162 (1990). doi:10.1103/PhysRevLett.65.3162. URL http://prl.aps.org/abstract/PRL/v65/i25/p3162_1
61. M.T. Woodside, P.L. McEuen, Science **296**(5570), 1098 (2002). doi:10.1126/science.1069923. URL http://www.ncbi.nlm.nih.gov/pubmed/12004123
62. J. Zhu, M. Brink, P.L. McEuen, Appl. Phys. Lett. **87**, 242102 (2005)
63. J. Zhu, M. Brink, P.L. McEuen, Nano Lett. **8**(8), 2399 (2008). URL http://pubs.acs.org/doi/abs/10.1021/nl801295y
64. R. Stomp, Y. Miyahara, S. Schaer, Q. Sun, H. Guo, P. Grutter, S. Studenikin, P. Poole, A. Sachrajda, Phys. Rev. Lett. **94**(5), 56802 (2005). doi:10.1103/PhysRevLett.94.056802. URL http://link.aps.org/doi/10.1103/PhysRevLett.94.056802
65. Y. Azuma, M. Kanehara, T. Teranishi, Y. Majima, Phys. Rev. Lett. **96**(1), 16108 (2006). doi:10.1103/PhysRevLett.96.016108. URL http://link.aps.org/doi/10.1103/PhysRevLett.96.016108
66. L. Cockins, Y. Miyahara, S.D. Bennett, A.A. Clerk, S. Studenikin, P. Poole, A. Sachrajda, P. Grutter, PNAS **107**(21), 9496 (2010). doi:10.1073/pnas.0912716107. URL http://www.pnas.org/cgi/content/abstract/107/21/9496
67. S.D. Bennett, L. Cockins, Y. Miyahara, P. Grütter, A.A. Clerk, Phys. Rev. Lett. **104**(1), 2 (2010). doi:10.1103/PhysRevLett.104.017203. URL http://link.aps.org/doi/10.1103/PhysRevLett.104.017203
68. L. Gross, F. Mohn, P. Liljeroth, J. Repp, F.J. Giessibl, G. Meyer, Science **324**(5933), 1428 (2009). URL http://www.sciencemag.org/cgi/content/abstract/324/5933/1428
69. H. Hölscher, B. Gotsmann, W. Allers, U. Schwarz, H. Fuchs, R. Wiesendanger, Phys. Rev. B **64**(7), 1 (2001). URL http://link.aps.org/doi/10.1103/PhysRevB.64.075402
70. A. Pioda, S. Kicin, T. Ihn, M. Sigrist, A. Fuhrer, K. Ensslin, A. Weichselbaum, S.E. Ulloa, M. Reinwald, W. Wegscheider, Phys. Rev. Lett. **93**, 216801 (2004)
71. P. Fallahi, A.C. Bleszynski, R.M. Westervelt, J. Huang, J.D. Walls, E.J. Heller, M. Hanson, A.C. Gossard, Nano Lett. **5**, 223 (2005)

72. A.C. Bleszynski, F.A. Zwanenburg, R.M. Westervelt, A.L. Roest, E.P.A.M. Bakkers, L.P. Kouwenhoven, Nano Lett. **7**(9), 2559 (2007). URL http://www.ncbi.nlm.nih.gov/pubmed/17691848
73. E. Bussmann, D.J. Kim, C.C. Williams, Appl. Phys. Lett. **85**(13), 2538 (2004). URL http://link.aip.org/link/APPLAB/v85/i13/p2538/s1&Agg=doi
74. E. Bussmann, C.C. Williams, Appl. Phys. Lett. **88**, 263108 (2006). URL http://link.aip.org/link/?APPLAB/88/263108/1
75. E.B. Bussmann, N. Zheng, C.C. Williams, Nano Lett. **6**(11), 2577 (2006). doi:10.1021/nl0620076. URL http://www.ncbi.nlm.nih.gov/pubmed/17090094
76. J.P. Johnson, N. Zheng, C.C. Williams, Nanotechnology **20**(5), 55701 (2009). URL http://stacks.iop.org/0957-4484/20/055701
77. N. Zheng, J.P. Johnson, C.C. Williams, G. Wang, Nanotechnology **21**(29), 295708 (2010). doi:10.1088/0957-4484/21/29/295708. URL http://www.ncbi.nlm.nih.gov/pubmed/20601769
78. W. Lu, Z. Ji, L. Pfeiffer, K.W. West, A.J. Rimberg, Nature **423**(6938), 422 (2003). URL http://dx.doi.org/10.1038/nature01642
79. R.G. Knobel, A.N. Cleland, Nature **424**(6946), 291 (2003). URL http://dx.doi.org/10.1038/nature01773
80. A. Yacoby, H.F. Hess, T.A. Fulton, L.N. Pfeiffer, K.W. West, Solid State Commun. **111**(1), 1 (1999). doi:10.1016/S0038-1098(99)00139-8. URL http://linkinghub.elsevier.com/retrieve/pii/S0038109899001398
81. N.B. Zhitenev, T.A. Fulton, A. Yacoby, H.F. Hess, L.N. Pfeiffer, K.W. West, Nature **404**(6777), 473 (2000). URL http://dx.doi.org/10.1038/35006591
82. S. Ilani, J. Martin, E. Teitelbaum, J.H. Smet, D. Mahalu, V. Umansky, A. Yacoby, Nature **427**(6972), 328 (2004). doi:10.1038/nature02230. URL http://www.ncbi.nlm.nih.gov/pubmed/14737162
83. J. Martin, N. Akerman, G. Ulbricht, T. Lohmann, J.H. Smet, K. von Klitzing, A. Yacoby, Nat. Phys. **4**(2), 144 (2007). doi:10.1038/nphys781. URL http://www.nature.com/doifinder/10.1038/nphys781
84. H.T.A. Brenning, S.E. Kubatkin, D. Erts, S.G. Kafanov, T. Bauch, P. Delsing, Nano Lett. **6**(5), 937 (2006). URL http://dx.doi.org/10.1021/nl052526t
85. P.I. Glicofridis, Subsurface charge accumulation imaging of the quantum hall liquid. Ph.D. thesis, Massachusetts Institute of Technology (2001)
86. G. Finkelstein, P. Glicofridis, R. Ashoori, M. Shayegan, Science **289**(5476), 90 (2000). doi:10.1126/science.289.5476.90. URL http://www.sciencemag.org/cgi/content/abstract/289/5476/90
87. I. Maasilta, S. Chakraborty, I. Kuljanishvili, S. Tessmer, M. Melloch, Phys. Rev. B **68**(20), 205328 (2003). doi:10.1103/PhysRevB.68.205328. URL http://link.aps.org/doi/10.1103/PhysRevB.68.205328
88. G.A. Steele, R.C. Ashoori, L.N. Pfeiffer, K.W. West, Phys. Rev. Lett. **95**(13), 136804 (2005)
89. I. Kuljanishvili, C. Kayis, J.F. Harrison, C. Piermarocchi, T.A. Kaplan, S.H. Tessmer, L.N. Pfeiffer, K.W. West, Nat. Phys. **4**(3), 227 (2008). URL http://dx.doi.org/10.1038/nphys855
90. M.P. Blencowe, Contemp. Phys. **46**(4), 249 (2005). URL http://www.informaworld.com/openurl?genre=article&doi=10.1080/00107510500146865&magic=crossref||D404A21C5BB053405B1A640AFFD44AE3
91. T.J. Kippenberg, K.J. Vahala, Science **321**(5893), 1172 (2008)